Journal of ELECTRONIC MATERIALS, Vol. 48, No. 4, 2019
https://doi.org/10.1007/s11664-018-06866-0

TOPICAL COLLECTION: INTERNATIONAL CONFERENCE ON THERMOELECTRICS 2018

Thermoelectric and Transport Properties of *n*-type Palladium-Doped Chalcopyrite $Cu_{1-x}Pd_xFeS_2$ Compounds

JIŘÍ NAVRATIL,[1,2,3] JANA KAŠPAROVÁ,[2] TOMÁŠ PLECHÁČEK,[2] LUDVÍK BENEŠ,[2] ZUZANA OLMROVÁ-ZMRHALOVÁ,[2] VLADIMÍR KUCEK,[2] and ČESTMÍR DRAŠAR[2]

1.—Institute of Macromolecular Chemistry, Academy of Sciences of the Czech Republic, Heyrovsky Sq. 2, 120 06 Prague, Czech Republic. 2.—Faculty of Chemical Technology, University of Pardubice, Studentská 573, 532 10 Pardubice, Czech Republic. 3.—e-mail: jiri.navratil@upce.cz

Semiconducting $CuFeS_2$ with a diamond-like structure has been recently studied as a potential candidate for thermoelectric applications. In the present study, Pd substitution for Cu was examined in terms of thermoelectric properties. A series of Pd-doped $Cu_{1-x}Pd_xFeS_2$ (x = 0–0.1) samples were synthesized. The thermoelectric and transport properties of hot-pressed sample pellets were characterized. We observed three effects: (1) Pd substituted for Cu behaves as an effective donor, increasing the free electron concentration. (2) Formation of the foreign phase—PdS—was observed above the solubility limit of Pd in $CuFeS_2$ ($x \geq 0.02$). (3) Segregation of the foreign phase is accompanied by the formation of Fe_{Cu}^{2+} antisite defects. All these effects synergically enhanced both the power factor $S^2{\cdot}\sigma$ and the thermoelectric parameter ZT. The highest values of the power factor ($\sim$ 1 mW m^{-1} K^{-1}) and the ZT parameter ($\sim$ 0.19 at 573 K) were achieved in the $Cu_{0.9}Pd_{0.1}FeS_2$ sample.

Key words: $CuFeS_2$, chalcopyrite, palladium, doping, thermoelectrics

INTRODUCTION

With the recent growth in global energy demand, the need for the development of alternative sources of energy, especially those that are renewable, is becoming urgent. The large amount of waste heat generated by various industrial processes and human activities represents one such renewable energy source, which will be difficult to ignore in the future. Thermoelectric (TE) technology, which directly converts waste heat into electrical energy via the Seebeck effect, represents one of the promising green alternatives for waste heat harvesting. One of the important research imperatives in the field of thermoelectrics is the quest for new inorganic compounds that are environmentally benign, nontoxic, low cost and composed of elements that are abundant on the Earth, while also meeting large-scale industrial requirements.

Chalcopyrite $CuFeS_2$ represents one of the compounds that meets most of the criteria and has been investigated for its potential thermoelectric applications.[1] This compound represents one of the minerals from the Cu-Fe-S family, and its abundance makes it the most important source of copper ore. Chalcopyrite that crystalizes in the tetragonal space group $I\bar{4}2d$ represents a natural extension of the II–VI ZnS compound, where Cu and Fe ions alternatively occupy the Zn site of the zinc-blende structure. Ternary $CuFeS_2$ is an antiferromagnetic semiconductor with a Néel temperature of 823 K.[2] It is a direct band gap semiconductor of *n*-type conductivity because of the intrinsic sulfur vacancy defects. Its band gap, determined by optical absorption measurements, is approximately 0.575 eV.[3]

The performance of thermoelectric materials can be measured by the dimensionless figure of merit, $ZT = S^2{\cdot}\sigma{\cdot}T/\kappa$, where S, σ, T, and κ are the Seebeck coefficient, the electrical conductivity, the

(Received August 21, 2018; accepted December 7, 2018; published online January 4, 2019)

temperature, and the thermal conductivity, respectively. The term $S^2{\cdot}\sigma$ is called the power factor, which is also an important figure for power generation in the case of harvesting large amounts of waste heat from various industrial processes.

$CuFeS_2$ has been recently reported as a material with reasonably high power factor values of approximately 1 mW m^{-1} K^{-1}.[1,4–7] The electronic structure of $CuFeS_2$, investigated in a number of theoretical studies,[8–10] confirmed the stability of the antiferromagnetic phase. Recent first-principle studies[11,12] suggested a possible enhancement of TE performance of this material, especially by a dilute doping.

The enhanced thermoelectric performance of $CuFeS_2$ by Co substitution in the Cu sublattice was reported in Ref. 13. In Ref. 14, the authors broadened the study of Tsuji et al.[5] utilizing the *in situ* formation of ZnS nanoinclusions in $Cu_{1-x}Zn_xFeS_2$ above the solubility limit of Zn substitution for Cu atoms in the system. The synergistic effect of Zn-doping and the presence of the ZnS nanophase additionally reduced the lattice thermal conductivity and led to the enhancement of the ZT value up to 0.26 at 630 *K* for $Cu_{0.92}Zn_{0.08}FeS_2$.

In this work, we present a study of a series of $Cu_{1-x}Pd_xFeS_2$ (x = 0–0.1) compounds. We show that Pd substituted for Cu in $Cu_{1-x}Pd_xFeS_2$ behaves as a donor but shows quite low solubility. Above the solubility limit, the PdS phase precipitates within the chalcopyrite matrix. PdS precipitates in the form of nanoinclusions at low Pd contents, and then, its grains grow larger at higher Pd contents. The formation of PdS is accompanied by the formation of AS defects in Fe_{Cu}^{2+}.

EXPERIMENTAL

Polycrystalline samples with the nominal composition of $Cu_{1-x}Pd_xFeS_2$ (x = 0, 0.01, 0.02, 0.03, 0.05, 0.07 and 0.1) were synthesized from a mixture of pure elements obtained from Sigma-Aldrich, including Cu (4 N shots), Pd (4 N powder), Fe (4 N granular) and S (5 N powder). The synthesis of the polycrystalline products was performed in evacuated ($\sim 10^{-3}$ Pa), sealed quartz ampoules. The ampoules were heated up to 1223 K over 10 h, maintained at this temperature for 24 h, and then slowly cooled to room temperature. The resulting ingot was then ground under acetone, pelletized and annealed at 923 K for 24 h. Then, it was slowly cooled (0.1 K min^{-1}) down to 673 K and then cooled to room temperature by switching off the furnace. The powder products were characterized by x-ray diffraction (XRD). The samples for physical characterization were compacted using hot-pressing at 763 K and 50 MPa for 1 h. Compacted disc-shaped samples (diameter 12 mm and thickness ca. 2 mm) were of ≥ 96% theoretical (x-ray) density as calculated from their mass and geometry.

The electrical conductivity σ was measured via the four-terminal method using an LSR-3 instrument (Linseis, Selb, Germany) from 300 K to 573 K on the disc-shaped samples. The Seebeck coefficient S was measured via the static DC method with the aid of the LSR-3 simultaneous with the measurement of electrical conductivity. The temperature gradient between two points was measured by two R-type thermocouples that were pressed against the sample surface. The measurements were performed under a He atmosphere under 0.1 bar overpressure.

The thermal diffusivity D was measured from 300 K to 573 K on the same round hot-pressed samples under an argon atmosphere using an LFA 457 instrument (NETZSCH-Gerätebau GmbH, Selb, Germany). The thermal conductivity κ was subsequently calculated using the relation $\kappa = D{\cdot}c_p{\cdot}\rho$, where c_p and ρ are the heat capacity and the experimental density, respectively. Inconel was used as the heat-capacity standard.

The Hall coefficient R_H was measured in the 300–573 K temperature range under a vacuum on the same samples that were used for the electrical conductivity measurements. The measurements were performed using an alternating current with a frequency of 1020 Hz and a stationary magnetic field with an induction of B = 0.5 T. Pressure-assisted mechanical current contacts and welded Pt-wire voltage contacts were used. The corresponding free carrier concentration N and free carrier mobility μ_H were calculated by the following equations: $N = 1/(e{\cdot}R_H)$ and $\mu_H = R_H{\cdot}\sigma$, where e is the electron charge.

The diffraction patterns (Cu Kα, λ = 1.5418 Å) of powdered samples were measured using a D8 Advance diffractometer (Bruker AXS, Germany) with a Bragg–Brentano Θ–Θ goniometer (radius 217.5 mm) equipped with a Ni-beta filter and LynxEye™ detector. The scan was performed at room temperature from 10° to 90° (2Θ) with a 0.01° step with a counting time of 1 s per step. The mass concentrations of the present phases were calculated by full pattern matching using EVA software.[15] For each selected pattern, EVA adjusts the scaling factor and width parameters by fitting, and the result is transformed into concentrations using the I/I_{cor} factors.[16]

The phases present in the samples were visualized with backscattered electrons using a scanning electron microscope Jeol JSM 5500 LV (JEOL Ltd., Tokyo, Japan) equipped with an energy dispersive x-ray (EDX) microanalyzer (IXRF Systems detector GRESHAM Sirius 10).

Differential thermal analysis (DTA) was performed using an R.M.I.-DTA 003 instrument (R.M.I. Electronic Measuring Instruments, Pardubice, Czech Republic) in a nonisothermal regime over a temperature range of 300–1070 K. A small quartz ampoule that contained a powdered sample ($\sim$ 50 mg) was evacuated to 10^{-3} Pa and heated and cooled using a heating/cooling rate of ± 10 K min^{-1}.

The temperature calibration was performed using pure metals: In, Sn, Pb, Zn and Al. A disc of sapphire was used for enthalpic calibration.

Thermogravimetric analysis (TGA) was carried out using a Pyris 1 TGA (PerkinElmer, Inc., USA) with a high-temperature furnace. The samples were placed in a platinum pan with a ceramic liner and heated from room temperature to 800°C at a heating rate of 10°C min^{-1} under a nitrogen atmosphere. The precision of the temperature measurement was 5°C.

RESULTS AND DISCUSSION

We used differential thermal analysis (DTA) and thermal gravimetry (TGA) to evaluate the thermal stability of the compounds and to estimate the temperature limit for their characterization. The results of these experiments are presented in Fig. 1. As frequently referred to in the literature,[17] the DTA results suggest that $CuFeS_2$ decomposes at 823 K to FeS_2 and an intermediate phase is referred to as the intermediate solid state (ISS). However, the results of TGA analysis show that the chalcopyrite starts to lose sulfur at temperatures as low as 600 K, which is why we ran all of our experiments only up to 573 K.

The XRD patterns collected from the synthesized powders before the hot-pressing process are presented in Fig. 2. All diffraction peaks can be indexed as tetragonal $CuFeS_2$ (JCPDS Card # 35-0752) up to a nominal concentration of Pd $x < 0.02$. Exceeding this concentration, XRD detects tetragonal phase PdS (JCPDS Card # 25-1234) as shown in the inset of Fig. 2 showing the magnified patterns in the range of 30–36 (2Θ) compared with the calculated pattern of PdS (bottom pattern in the inset). Scanning electron microscopy (SEM) in backscattered electron mode (BSE) revealed PdS particles (light blue dots in Fig. 3) within the chalcopyrite (CP) matrix (darker blue area in Fig. 3). In addition to larger precipitates, we observed a large number of inclusions of approximately 100 nm in size. The particle morphology, along with dimensions and characteristic distribution, is very similar to that in the study of Ref. 14. In this study, the authors investigated Zn-doped $Cu_{1-x}Zn_xFeS_2$ samples in the same nominal composition range, i.e., x = 0–0.1, as in the present paper. The authors observed a lowering of the dimensions of precipitated ZnS particles with decreasing nominal concentrations of Zn. At the lowest nominal Zn concentrations, when ZnS started to precipitate from the CP matrix, they observed the formation of ZnS nanoinclusions with an average size of a few tens of nanometers by

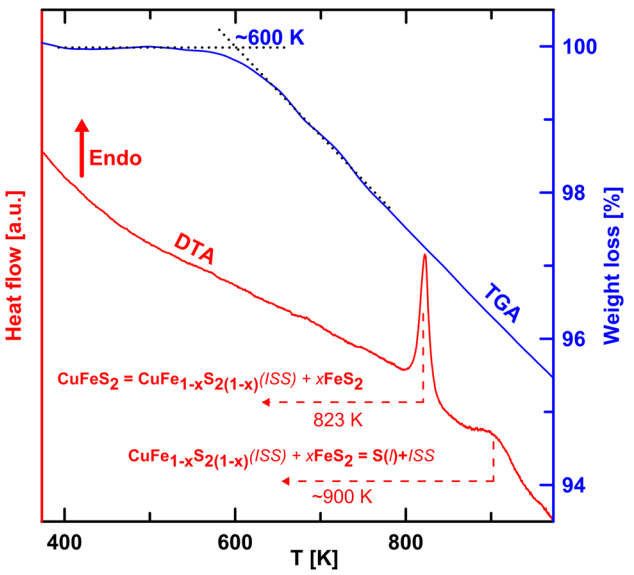

Fig. 1. Differential thermal analysis (red line) and thermal gravimetry (blue line) data of the undoped $CuFeS_2$ powder (Color figure online).

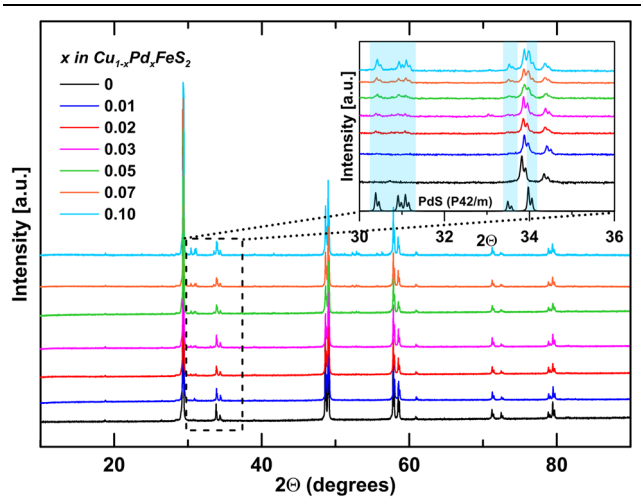

Fig. 2. Powder XRD patterns of $Cu_{1-x}Pd_xFeS_2$ (x = 0, 0.01, 0.02, 0.03, 0.05, 0.07, and 0.1) samples. The right inset is a magnified graph at 2θ ranging from 30° to 36° compared with the calculated XRD pattern of PdS, which is presented at the bottom of the inset.

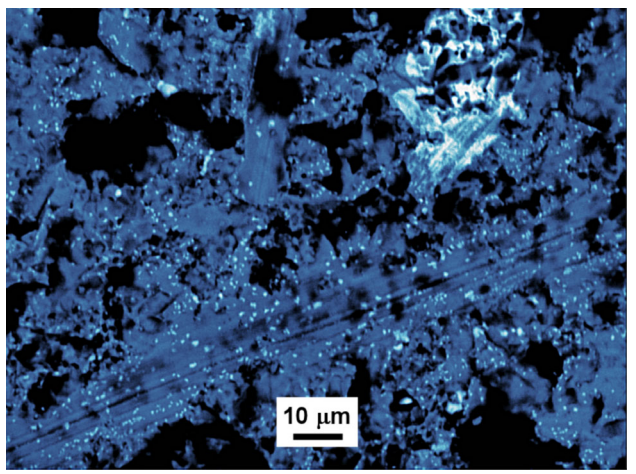

Fig. 3. Backscattered electron SEM image of the $Cu_{0.9}Pd_{0.1}FeS_2$ sample. As confirmed by EDX analysis, the light blue spots correspond to the PdS phase. The dark blue area belongs to the matrix chalcopyrite phase (Color figure online).

high-resolution transmission electron microscopy (HRTEM). We assume that PdS forms similar nanoinclusions in our samples in regions of low Pd concentrations. The broadening of PdS diffraction peaks with decreasing nominal concentration of Pd corroborates this assumption.

The content of the PdS phase present in the CP matrix was determined using EVA software.[15] The results of the calculations are summarized in Table I. Figure 4a, shows the experimental concentration of PdS in samples (red line) is lower than the theoretical concentration (black line) by a constant, assuming that all added Pd does react with sulfur to form PdS. Extrapolation of the red line provides an estimation of the solubility limit of Pd in a $Cu_{1-x}Pd_xFeS_2$ series (Fig. 4a). Thus, we estimated the solubility limit to be slightly above $x = 0.01$, i.e., Pd is able to substitute approximately 1% of the Cu atoms in the $Cu_{1-x}Pd_xFeS_2$ system. A more detailed analysis of the obtained x-ray patterns presented in Table I reveals that the lattice parameters a and c (and also the corresponding unit-cell volume V) of the matrix (chalcopyrite) phase increase almost linearly with increasing nominal content of Pd in the samples (see Fig. 4b). The only exception is the sample with the lowest nominal concentration of Pd, i.e., $Cu_{0.99}Pd_{0.01}FeS_2$. Its lattice parameters are the same as those of the undoped $CuFeS_2$ sample. Note that we assume that all Pd atoms enter the Cu sublattice for this sample. The Pd-concentration is very low, and the ionic radii of Cu^+ and Pd^{2+} ions are quite similar, i.e., 77 pm versus 86 pm.[18] At and above this nominal concentration, the spare Pd reacts *in situ* with a corresponding quantity of sulfur, and the PdS phase starts to precipitate inside the chalcopyrite matrix. As follows from the reaction stoichiometry (Eq. 1), the formation of the PdS phase implies an increasing deficiency of copper and sulfur in the matrix compounds, which induces a shift of Fe atoms onto Cu sites, i.e., Cu atoms are substituted by the formation of Fe_{Cu}^{2+} antisite (AS) defects as proposed in Ref. 14. This conclusion is corroborated by the solid coincidence of a linear increase in lattice parameters (along with both their magnitudes and slopes) observed in the present work and in Li's work studying the thermoelectric properties of $Cu_{1-x}Fe_{1+x}S_2$ compounds.[6] The samples with the higher nominal concentration ($x = 0.1$) contain small but unquantifiable amounts of FeS_2 phase.

The room-temperature values of transport properties for all studied samples are summarized in Table II. In Fig. 5, we present the electrical conductivity σ (Fig. 5a), the Seebeck coefficient S (Fig. 5b) and the power factor $S^2{\cdot}\sigma$ (Fig. 5c) as a function of temperature in the 300–573 K range. The increase in the electrical conductivity with increasing nominal content of Pd is mostly due to an increase in free carrier concentration. The absolute values of the Seebeck coefficient decrease with increasing nominal content of Pd. While the electrical conductivity of the undoped $CuFeS_2$ sample shows semiconducting behavior at lower temperatures, the σ-values of the other samples decrease monotonically with temperature, suggesting a degenerate state. The negative values of the Seebeck coefficient (see Fig. 5b) indicate that all the samples are n-type and that electrons dominate their transport properties. Interestingly, the calculated values of the power factor $S^2{\cdot}\sigma$, plotted in Fig. 5c as a function of T, are almost temperature independent in the measured temperature region. They increase with the Pd content up to $x = 0.05$ (with the exception of 0.03) and then stay more or less constant, reaching values close to 1 mW m^{-1} K^{-2}.

The free carrier concentration n was determined from measurements of the Hall coefficient $R_H = 1/ne$, where R_H is the Hall coefficient and e is the electron charge. The values of Hall mobility μ_H of the samples were calculated as a product of the Hall coefficient and the electrical conductivity, i.e., $R_H{\cdot}\sigma$. The room-temperature values of both parameters are given in Table II. By plotting their values against the nominal content of Pd (see Fig. 6), the mobility of the samples steeply decreases at first, reaching a minimum at $x = 0.05$ and then slightly increases again. As we show below, the steep decrease is caused by the fact that an electron's effective mass gets heavier with the increasing

Table I. The measured lattice parameters (a, c, V) and the results of the quantitative phase analysis based on the Reference Intensity Ratio (RIR) method for $Cu_{1-x}Pd_xFeS_2$ (x = 0, 0.01, 0.02, 0.03, 0.05, 0.07 and 0.1) samples

	Lattice parameters $Cu_{1-x}Pd_xFeS_2$			Phase analysis using EVA (wt.%)		
x	a (Å)	c (Å)	V (Å)	$CuFeS_2$	PdS	FeS_2
0.00	5.28913	10.41994	291.4967	100	–	–
0.01	5.28904	10.41984	291.4840	100	–	–
0.02	5.28935	10.42396	291.6335	100	+	–
0.03	5.28959	10.42444	291.6734	98.3	1.5	–
0.05	5.28988	10.42808	291.8072	97.0	3.0	–
0.07	5.29053	10.43144	291.9730	95.9	4.1	–
0.10	5.29126	10.43653	292.1960	93.5	6.5	+

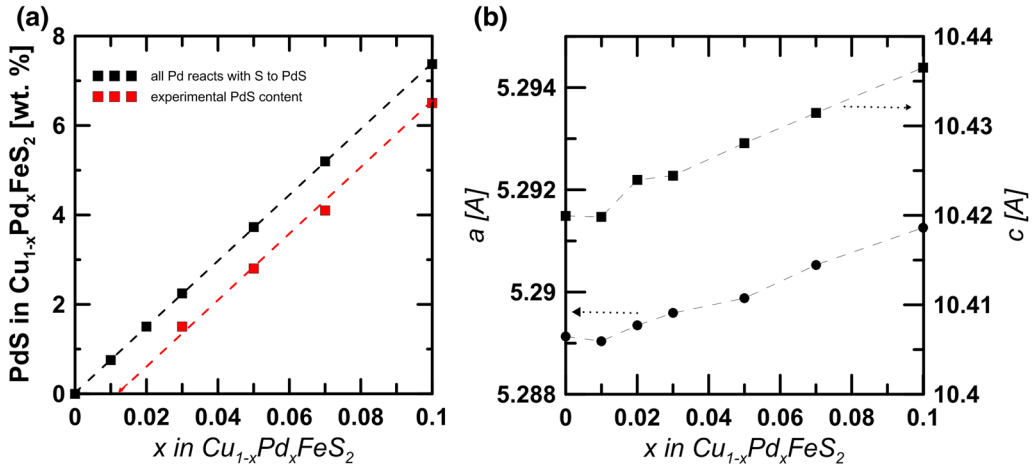

Fig. 4. (a) Experimentally determined PdS content (red squares) in the CP-PdS composites compared with the theoretical case of unlimited solubility of Pd in $Cu_{1-x}Pd_xFeS_2$ samples (black squares). From the extrapolation of the experimental results, one can estimate the solubility limit of Pd in the samples. (b) Lattice parameters of $Cu_{1-x}Pd_xFeS_2$ (Color figure online).

Table II. Room temperature transport parameters for $Cu_{1-x}Pd_xFeS_2$ (x = 0, 0.01, 0.02, 0.03, 0.05, 0.07 and 0.1) samples

x	σ (S m^{-1})	S (μV K^{-1})	R_H (cm^3 C^{-1})	$n = 1/(R_H \cdot e)$ (10^{18} cm^{-3})	μ_H (cm^2 V^{-1} s^{-1})
0.00	2880	− 422	− 0.868	0.72	25.0
0.01	5925	− 376	− 0.193	3.22	11.4
0.02	9510	− 300	− 0.104	6.00	9.9
0.03	11,910	− 253	− 0.071	8.79	8.5
0.05	19,485	− 228	− 0.034	18.1	6.6
0.07	23,675	− 201	− 0.029	21.2	6.9
0.10	27,765	− 178	− 0.026	23.7	7.2

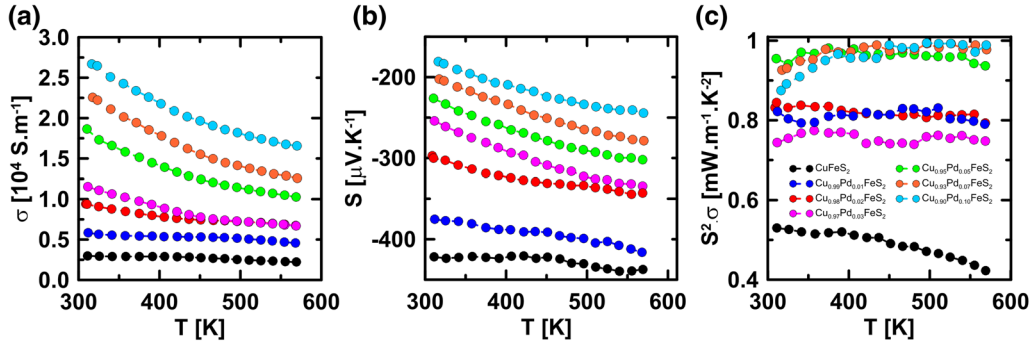

Fig. 5. (a) Electrical conductivity, (b) Seebeck coefficient and (c) power factor of $Cu_{1-x}Pd_xFeS_2$ samples as a function of temperature.

concentration of free carriers. The further increase is probably connected with the increasing content of the PdS phase in the composite samples. Namely, polycrystalline PdS shows much higher mobility (230 cm^2 V^{-1} s^{-1}) than CP.[19] Interestingly, the free carrier concentration (FCC) increases almost linearly with the nominal composition of Pd (Fig. 6).

The plot of the Seebeck coefficient S as a function of the carrier concentration n (Pisarenko plot) is depicted in Fig. 7a. The plot compares experimental values of the Seebeck coefficient (circles) with theoretical values (dashed lines) calculated for a single parabolic band and dominating the acoustic scattering of free carriers. As shown in Fig. 7a, the effective mass m^* becomes heavier with increasing concentrations of free carriers. This effect, observed by other authors,[6,14] can be explained in the following manner. The edge states of the conduction band are mostly composed of 3p-orbitals of sulfur.[10] However, slightly above the edge, the d-orbitals of Fe dominate. Thus, the free carriers close to the edge (low FCC) show a lower effective mass, while

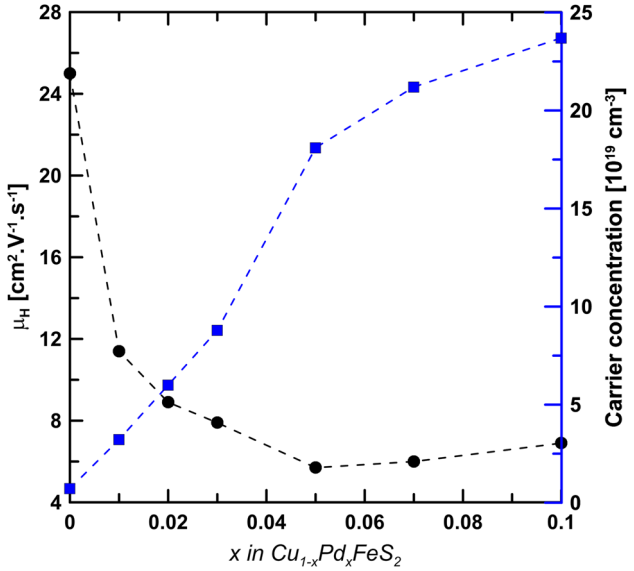

Fig. 6. Room-temperature values of the carrier mobility (black circles) and the free carrier concentration (blue squares) as a function of the nominal doping content at room temperature in the $Cu_{1-x}Pd_xFeS_2$ system. The dashed lines are only to guide the eyes (Color figure online).

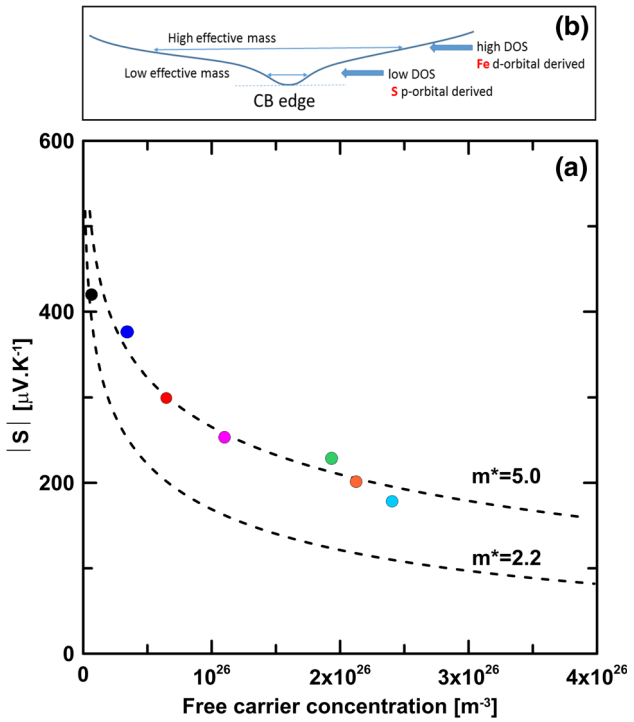

Fig. 7. (a) Pisarenko plots (Seebeck coefficient versus free carrier concentration) at 300 K. The dashed black lines are based on a model employing a single parabolic band with an effective masses $m^* = 2.2\ m_e$ and $m^* = 5.0\ m_e$ assuming an acoustic phonon scattering mechanism ($r = -1/2$), respectively. (b) The scheme of DOS for the edge of the conduction band showing lower DOS at the very edge of the band due to sulfur domination. Note that one would obtain much lower effective masses assuming another scattering mechanism. Namely, mixed ionized impurities and acoustic phonons would provide much lower effective masses.

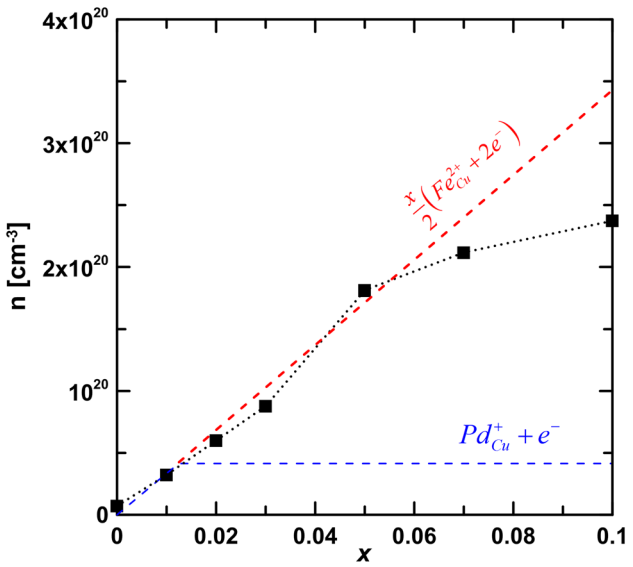

Fig. 8. Carrier concentration as a function of the nominal doping at room temperature in the $Cu_{1-x}Pd_xFeS_2$ system. The dashed lines represent the theoretical models where full ionization is assumed (one electron carrier per dopant atom). The blue dashed line corresponds to the theoretical contribution of charged Pd^+_{Cu} defects below the solubility limit of Pd in $Cu_{1-x}Pd_xFeS_2$. The red dashed line represents the theoretical contribution of arising Fe^{2+}_{Cu} AS defects according to Eq. 1 (Color figure online).

the effective mass increases with increasing FCC due to merging into high DOS originating from Fe *d*-orbitals, as schematically depicted in Fig. 7b.

In Fig. 8, we show a picture of variations of the FCC for $Cu_{1-x}Pd_xFeS_2$ samples in terms of present point defects. For the undoped $CuFeS_2$ sample, the quite low FCC ($\sim 7.2 \times 10^{17}$ cm^{-3}) originates from the presence of positively charged sulfur vacancies V_S^{2+} liberating two electrons per vacancy. In the area below the solubility limit α, determined in this work to be approximately $x = 0.013$ (Fig. 4a), all Pd atoms substitute for Cu atoms forming positively charged Pd^+_{Cu} defects compensated by one electron. The model in Fig. 8 (dashed blue line) nicely matches the experimental data in the area of low FCC. However, above the solubility limit, all Pd reacts with the sulfur to form the PdS phase. Simultaneously, some Fe atoms enter Cu sites, forming Fe^{2+}_{Cu} AS defects to maintain cation/anion stoichiometry and to relax the lattice strain due to the increasing deficiency of the sulfur in the CP matrix. The following equation summarizes the situation:

$$Cu_{1-x-\alpha}Pd_{\alpha+x}FeS_2 \rightarrow xPdS + Cu_{1-x-\alpha}Pd_\alpha FeS_{2-x} \rightarrow xPdS + Cu(Fe)_{1-x/2-\alpha}Pd_\alpha Fe_{1-x/2}S_{2-x}. \quad (1)$$

The last term of the equation describes the formation of AS defects. Note that the last formula in Eq. 1 maintains the 1:1:2 stoichiometry of the

matrix compound. The red dashed line in Fig. 8 represents the model describing the theoretical contribution arising from Fe_{Cu}^{2+} AS defects. The model corresponds well to the experimental dependence x versus n up to $x \sim 0.05$. At higher x, an increase in the experimental FCC values becomes slower compared to the model. The reason for this slowdown at higher x is most likely connected with increasing content of the foreign phases (PdS and FeS_2).

Figure 9a shows the total thermal conductivity κ as a function of temperature for all samples. The decrease in κ with increasing temperature for all the samples is mainly due to the enhanced contribution of the Umklapp processes. The thermal conductivity also decreases with increasing x with the exception of sample $Cu_{0.95}Pd_{0.05}FeS_2$. Considering only two main components contribute to κ, i.e., the electronic (κ_{el}) and lattice (κ_L) parts of the thermal conductivity, we calculated κ_{el} using the Wiedemann–Franz relation. The latter component was determined by subtracting κ_{el} from κ. The Lorentz number L from the Wiedemann–Franz relation $\kappa_{el} = L \cdot \sigma \cdot T$, where σ is the electrical conductivity and T is the temperature, was estimated from Eq. 2, assuming a single parabolic band model and acoustic phonon scattering as the prevailing carrier-scattering mechanism.

$$L = \left(\frac{k_B}{e}\right)^2 \left(\frac{(r+7/2)F_{r+5/2}(\eta)}{(r+3/2)F_{r+1/2}(\eta)} - \left[\frac{(r+5/2)F_{r+3/2}(\eta)}{(r+3/2)F_{r+1/2}(\eta)}\right]^2 \right) \quad (2)$$

The reduced Fermi energy η was obtained by fitting the experimental Seebeck coefficient (S) values according to Eq. 3 as follows:

$$S = \pm \frac{k_B}{e} \left(\frac{(r+5/2)F_{r+3/2}(\eta)}{(r+3/2)F_{r+1/2}(\eta)} - \eta \right), \text{ where} \quad (3)$$

$$F_n(\eta) = \int_0^\infty \frac{x}{1+e^{x-\eta}}\, dx \text{ is the Fermi integral.} \quad (4)$$

Here, k_B and e are the Boltzmann constant and the charge of an electron, respectively, and r is the scattering factor. For acoustic scattering, the value $r = -1/2$ applies.[20] The Lorentz number was practically the same for all samples, i.e., $L = 1.5 \times 10^{-8}$ W Ω K^{-2}. The calculated electronic part of the thermal conductivity κ_{el} as a function of temperature is shown in Fig. 9b. Although its value slightly increases with increasing x, its contribution to the total thermal conductivity is marginal and reaches at most a few percent. Thus, the thermal conductivity of the studied $Cu_{1-x}Pd_xFeS_2$ samples is dominated mainly by its lattice part κ_L. The calculated values of κ_L are presented in Fig. 9c. Plotting the room-temperature values of the lattice thermal conductivity κ_L against the nominal concentration x (see Fig. 10), we obtained a very similar picture to that in Ref. 14 for the $Cu_{1-x}Zn_xFeS_2$ system; κ_L decreased with increasing x up to $x = 0.03$, then increased between 0.03 and 0.05, followed by a further decrease in κ_L again. In the context of the previous discussion, we distinguish three different regions in the plot. In the first one (light blue), spreading from $x = 0$ up to the solubility limit of Pd in $Cu_{1-x}Pd_xFeS_2$, we assume the full substitution of Cu atoms by Pd. In region II (pink one), the PdS phase precipitates in the CP matrix, followed by the formation of Fe_{Cu}^{2+} AS defects. In this region, the changes in κ_L reflect the formation of PdS precipitates of very small size. In region III (light green), the influence of scattering on the AS defects prevails over the scattering on the PdS inclusions. To verify this scenario, we theoretically calculated the κ_L values using two theoretical models. We first utilized the Callaway model to judge the contribution of the point defect scattering in the CP matrix on κ_L and then the effective medium theory (EMT) to judge the effect of the CP-PdS composite formation on κ_L.

The Callaway model[21] derived for calculation of κ_L above the Debye temperature Θ_D ignoring phonon grain boundary scattering and considering Umklapp and point defect phonon scattering processes allows calculation of the κ_L of a disordered

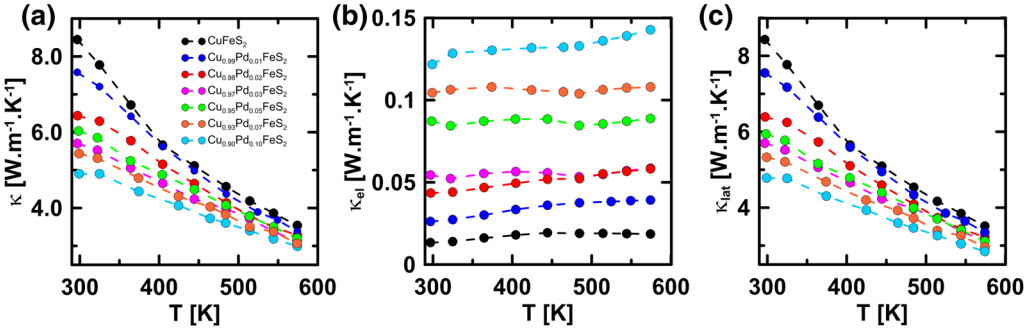

Fig. 9. Temperature dependence of (a) the total thermal conductivity κ, (b) the calculated electronic part κ_{el} and (c) the lattice thermal conductivity κ_L of $Cu_{1-x}Pd_xFeS_2$ samples.

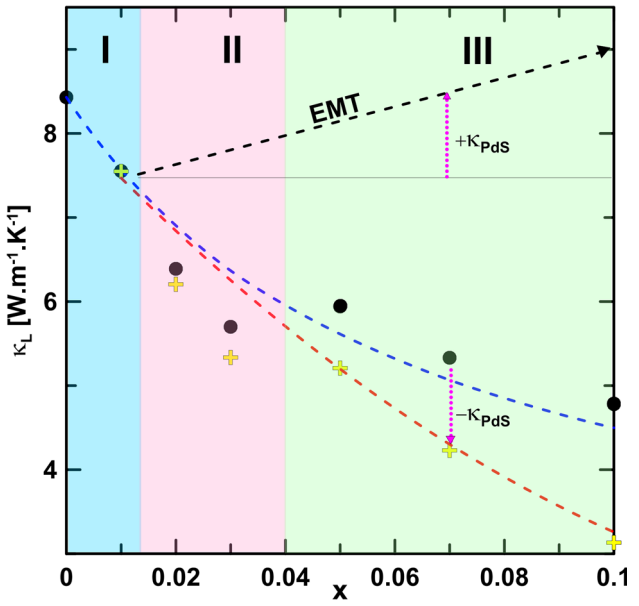

Fig. 10. Room-temperature lattice thermal conductivity κ_L as a function of the nominal doping content (black circles) at room temperature in the $Cu_{1-x}Pd_xFeS_2$ system. The blue dashed line represents the theoretical change in κ_L based on the Callaway model due to full Pd substitution for Cu atoms (using the value $\varepsilon_1 = 200$ calculated from Eq. 11). The black dashed line corresponds to the theoretical contribution of κ_L due to the presence of PdS inclusions in the CP matrix as calculated by the EMT model according to Eq. 12. The yellow crosses represent the corrected κ_L values after elimination of the PdS contribution to the κ_L of the composites. The red dashed line represents the results of the Callaway model due to the formation of Fe^{2+}_{Cu} AS defects (the ε_1 parameter was adjusted to satisfy $\Gamma_{exp} = \Gamma_{calc} = \Gamma_M + \Gamma_S$ condition it the region $0.05 \le x \le 0.01$) (Color figure online).

compound ($Cu_{1-x}Pd_xFeS_2$) from the following relation:

$$\frac{\kappa_L}{\kappa_L^P} = \frac{\tan^{-1}(u)}{u}, \quad u^2 = \frac{\pi\,\Theta_D\Omega}{hv^2}\kappa_L^P\Gamma, \tag{5}$$

where κ_L^P is the lattice thermal conductivity of the compound without disorder (in our case, undoped $CuFeS_2$). u, h, Ω, v and Γ are disorder scaling parameters, the Planck constant, the average volume per 1 atom, the average sound velocity and the scattering parameter, respectively. The scattering parameter Γ_{calc} can be calculated from the model developed by Slack[22] and Abeles[23] as $\Gamma_{calc} = \Gamma_M + \Gamma_S$, where the scattering parameters Γ_M and Γ_S are related to the mass and strain field fluctuation, respectively. Both parameters can be expressed as follows:

$$\Gamma_M = \frac{\sum_{i=1}^{n} c_i \left(\frac{\overline{M_i}}{\overline{\overline{M}}}\right)^2 f_i^1 f_i^2 \left(\frac{M_i^1 - M_i^2}{\overline{M_i}}\right)^2}{\sum_{i=1}^{n} c_i}, \tag{6}$$

$$\Gamma_S = \frac{\sum_{i=1}^{n} c_i \left(\frac{\overline{M_i}}{\overline{\overline{M}}}\right)^2 f_i^1 f_i^2 \varepsilon_i \left(\frac{r_i^1 - r_i^2}{\overline{r_i}}\right)^2}{\sum_{i=1}^{n} c_i}, \tag{7}$$

where n is the number of different crystallographic sublattices in the structure and c_i are the relative degeneracies of the respective sites. In the case of $CuFeS_2$, there are three different crystallographic sublattices ($n = 3$), and their relative degeneracies are $c_1 = c_2 = 1$ and $c_3 = 2$. The above relations assume that two types of atoms can alternate on each ith sublattice. $\overline{\overline{M}}$ is the average atomic mass of the compound, and $\overline{M_i}$, $\overline{r_i}$ and ε_i are the average atomic mass, radius on the ith sublattice and a phenomenological adjustable parameter for the ith sublattice, respectively. They can be expressed as follows:

$$\overline{\overline{M}} = \frac{\sum_{i=1}^{n} c_i \overline{M_i}}{\sum_{i=1}^{n} c_i}, \tag{8}$$

$$\overline{M_i} = \sum_k f_i^k M_i^k, \tag{9}$$

$$\overline{r_i} = \sum_k f_i^k r_i^k. \tag{10}$$

The phenomenological adjustable parameter ε_i is always included because of the uncertainty of Γ_S. Frequently, it can be obtained either by the fitting of Γ_{exp} derived from Eq. 5 or estimated from the following equation[23]:

$$\varepsilon_i = 2(W + 6.4\gamma)^2, \tag{11}$$

where γ is the Grüneisen parameter and W is the ratio between the relative change in the bulk modulus and the strain. To calculate the theoretical change in κ_L due to Pd substitution in the Cu sublattice in the $Cu_{1-x}Pd_xFeS_2$ samples, we estimated the ε_1-value from Eq. 11 using values $\gamma = 1.1$ (mean value of $CuXS_2$ compounds published in Ref. 24) and $W = 3$, which was estimated for I–III–VI_2 chalcopyrite semiconductors in Ref. 25. The calculated value $\varepsilon_1 = 200$ was used for calculation of the theoretical κ_L using Eqs. 5–7. The model is presented as a blue dashed line in Fig. 10. It nicely describes the decrease in experimental values of κ_L in the area where substitution of Cu by Pd is expected, i.e., below the solubility limit.

As mentioned above, crossing the solubility limit of Pd in $Cu_{1-x}Pd_xFeS_2$, two other effects contribute to further changes in κ_L. First, the nonsubstituting Pd atoms react with sulfur, forming PdS inclusions in the CP matrix, and second, Fe^{2+}_{Cu} AS defects are formed to keep the cation/anion ratio close to 1. Knowing the content of PdS in the PdS-CP composite (see Table II), we calculated the theoretical change in κ_L by means of the effective medium theory (EMT) using the equation of the thermal conductivity of composites in Refs. 26 and 27. Thus, the effective value of lattice thermal conductivity

κ_{Leff} for the composite sample can be derived from the following equation:

$$(1-x_1)\frac{\kappa_{L1}-\kappa_{Leff}}{\kappa_{L1}+2\kappa_{Leff}}+x_1\frac{\kappa_{L2}-\kappa_{Leff}}{\kappa_{L2}+2\kappa_{Leff}}=0, \qquad (12)$$

where x_1 represents the volume fraction of the impurity (PdS) phase. As κ_{L1} (the lattice thermal conductivity of the matrix compound), we used the value κ_{L1} = 7.5 W m^{-1} K^{-1}, i.e., the value the studied system reached at the solubility limit. The value κ_2 = 24.2 W m^{-1} K^{-1} (for polycrystalline PdS) was taken from the work of Ref. 19. The model is presented in Fig. 10 by the black dashed line and actually represents the expected increase in κ_L in a macroscopic mixture of $Cu_{0.99}Pd_{0.01}FeS_2$-PdS composite. The increase is comparable with the results published in Ref. 14, where the authors intentionally prepared $CuFeS_2$-ZnS composite by a simple mixing of the components. This method allows us to separate the contribution of the PdS precipitates (κ_{PdS}) from the contribution due to the formation of the Fe_{Cu}^{2+} AS defects. As schematically illustrated in Fig. 10, the true contribution of AS defects was obtained by subtracting $\kappa_{Lexp} - \kappa_{PdS}$ values above the solubility limit, as depicted in Fig. 10 by yellow crosses. The nonmonotonous dependence hints at another effect contributing to the observed κ_L decrease. We assume that the steeper decrease in κ_L between the solubility limit and $x < 0.05$ is due to the formation of *in situ* nanoprecipitates of PdS. The enhanced boundary scattering of phonons on the nanoparticles further reduced κ_L. Although we were not able to observe the formation of the nanoparticles directly, we assume it is analogous with that observed in Ref. 14. They observed the presence of ZnS nanoprecipitates in the $Cu_{1-x}Zn_xFeS_2$ system. The radius of the nanoparticles increases with the increasing content of precipitated PdS in the CP-PdS composites, i.e., with increasing x in $Cu_{1-x}Pd_xFeS_2$ samples. After crossing a particular radius known as the Kapitza radius, the nanoparticle-induced reduction in κ_L is cancelled due to the presence of larger precipitates. Hence, the κ_L of the composite can be further treated according to the EMT model. The critical content lies around x = 0.05. This implies that the reduction in thermal conductivity is due to the formation of Fe_{Cu}^{2+} AS defects in the range $0.05 \le x \le 0.1$. We applied the Callaway model on this set of data again to evaluate the effect of the AS defects on κ_L. However, before applying the Callaway model, the contribution of PdS in the data was subtracted (yellow crosses in Fig. 10). We used Eq. 5 to calculate $\Gamma_{exp,}$ and then we calculated the scattering parameters Γ_M and Γ_S using Eqs. 6 and 7. The crystal radii of Cu^+ and Fe^{3+} for tetragonal coordination are listed in Ref. 18, and the ε_1 parameter was adjusted to satisfy the $\Gamma_{exp} = \Gamma_{calc} = \Gamma_M + \Gamma_S$ condition in the region $0.05 \le x \le 0.01$. In this way, we obtained a reduction in κ_L due to the formation of Fe_{Cu}^{2+} AS defects. As shown in Fig. 10, it reasonably corresponds to the experimental values corrected for the contribution of the κ_{PdS} (red dashed line). We found that $\Gamma_S \gg \Gamma_M$, and thus, we conclude that strain field fluctuation scattering dominates phonon scattering.

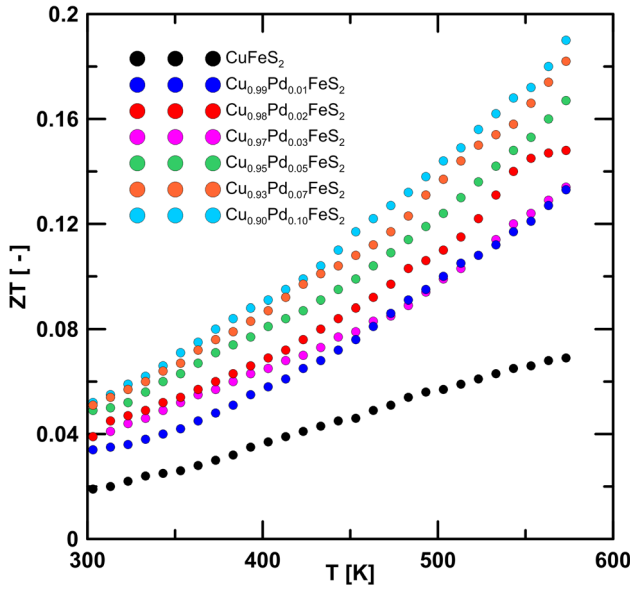

Fig. 11. ZT values of $Cu_{1-x}Pd_xFeS_2$ samples as a function of temperature.

Figure 11 shows the figure of merit $ZT = S^2 \cdot \sigma \cdot T/\kappa$ of $Cu_{1-x}Pd_xFeS_2$ as a function of temperature. The ZT parameter of all samples increases monotonically with increasing temperature and with a nominal concentration of Pd. The highest ZT value is obtained in the $Cu_{0.90}Pd_{0.10}FeS_2$ sample and reaches ZT = 0.19 at 573 K, which is comparable with the best ZT values achieved either by the $Cu_{1-x}Zn_xFeS_2$ system[14] or the $Cu_{1-x}Fe_{1+x}FeS_2$ system.[6]

We conclude that substitution slightly above the solubility limit can produce nanoprecipitates that are beneficial in lowering thermal conductivity. On the other hand, the formation of AS defects can induce favorable changes in both thermal and electronic transport. Thus, we anticipate that both a substitution into the Cu sublattice and an optimization of the Cu/Fe ratio in the $CuFeS_2$ matrix might be employed together to achieve better thermoelectric properties. Furthermore, the results of this paper suggest that the higher concentrations of PdS on *PF* are worth exploring.

CONCLUSIONS

In summary, a series of *n*-type $Cu_{1-x}Pd_xFeS_2$ samples were prepared by vacuum melting and subsequent hot-pressing. Pd displays a donor-like character when substituting for Cu. However, the solubility limit of Pd is rather low ($x \approx 0.013$). Above the solubility limit, the nonsubstituting Pd reacts with S, forming an *in situ* PdS phase inside the chalcopyrite matrix. At lower concentrations of Pd, the PdS phase is most likely present in the form of nanoinclusions that enhance phonon scattering and contribute to an additional reduction in κ_L. However, the PdS inclusions tend to grow with increasing Pd content. Upon crossing the critical diameter, the nanocomposite effectively turns into a microcomposite. From this point on, the presence of the PdS phase increases the κ_L due to the high thermal conductivity of PdS. With the formation of the PdS phase, a portion of the Fe atoms are forced to enter the Cu sublattice, forming Fe_{Cu}^{2+} antisite defects to re-establish the cation/anion ratio and to relieve the lattice strain. Donor behavior of this defect contributes to further variation in the transport properties. Increasing phonon scattering on the ionized impurities (Fe_{Cu}^{2+}) further reduces κ_L of the composites and more than compensates for the opposite effect of the PdS microprecipitates. We conclude that both the present point defects and the PdS phase may act in a synergistic manner to enhance the thermoelectric properties of the studied material. As a result, the highest values of the power factor (~ 1 mW m^{-1} K^{-2}) and the ZT parameter (~ 0.19 at 573 *K*) were achieved in the $Cu_{0.9}Pd_{0.1}FeS_2$ sample. However, we anticipate that light Pd substitution for Cu leading to nanoprecipitates together with an optimization of the Cu/Fe ratio might help to achieve better thermoelectric properties of $CuFeS_2$.

ACKNOWLEDGMENTS

Financial support from the Czech Science Foundation, Projects Nos. 16-07711S and 18-12761S, was greatly appreciated.

REFERENCES

1. N. Tsujii, *J. Electron. Mater.* 42, 1974 (2013).
2. M. DiGiuseppe, J. Steger, A. Wold, and E. Kostiner, *Inorg. Chem.* 13, 1828 (1974).
3. L. Barkat, N. Hamdadou, M. Morsli, A. Khelil, and J.C. Bernede, *J. Cryst. Growth* 297, 426 (2006).
4. J.H. Li, Q. Tan, and J.F. Li, *J. Alloy. Compd.* 551, 143 (2013).
5. N. Tsujii and T. Mori, *Appl. Phys. Express* 6, 043001 (2013).
6. Y. Li, T. Zhang, Y. Qin, T. Day, G.J. Snyder, X. Shi, and L. Chen, *J. Appl. Phys.* 116, 203705 (2014).
7. R. Ang, A.U. Khan, N. Tsujii, K. Takai, R. Nakamura, and T. Mori, *Angew. Chem. Int. Ed.* 54, 12909 (2015).
8. T. Hamajima, T. Kambara, K.I. Gondaira, and T. Oguchi, *Phys. Rev. B* 24, 3349 (1981).
9. M. Zhou, X. Gao, Y. Cheng, X.R. Chen, and L.C. Cai, *Appl. Phys. A Mater. Sci. Process.* 118, 1145 (2015).
10. S. Conejeros, P. Alemany, M. Llunell, I.P.R. Moreira, V. Sanchez, and J. Llanos, *Inorg. Chem.* 54, 4840 (2015).
11. H. Takaki, K. Kobayashi, M. Shimono, N. Kobayashi, K. Hirose, N. Tsujii, and T. Mori, *Mater. Today Phys.* 3, 85 (2017).
12. H. Takaki, K. Kobayashi, M. Shimono, N. Kobayashi, K. Hirose, N. Tsujii, and T. Mori, *Appl. Phys. Lett.* 110, 072107 (2017).
13. D. Berthebaud, O.I. Lebedev, and A. Maignan, *J. Materiomics* 1, 68 (2015).
14. H. Xie, X. Su, G. Zheng, T. Zhu, K. Yin, Y. Yan, C. Uher, M.G. Kanatzidis, and X. Tang, *Adv. Energy Mater.* 7, 1601299 (2017).
15. EVA, ver.19, Diffracplus Basic Evaluating Package. Bruker AXS GmbH (2013).
16. K.K. Wu, B. Ramachandran, Y.K. Kuo, R. Sankar, and F.C. Chou, *J. Alloy. Compd.* 682, 225–231 (2016).
17. L.J. Cabri, *Econ. Geol.* 68, 443 (1973).
18. R.D. Shannon, *Acta Crystallogr. Sect. A* 32, 751 (1976).
19. L.C. Chen, B.B. Jiang, H. Yu, H.J. Pang, L. Su, X. Shi, L.D. Chen, and X.J. Chen, *RSC Adv.* 8, 13154 (2018).
20. E. Conwell and V.F. Weisskopf, *Phys. Rev.* 77, 388 (1950).
21. J. Callaway and H.C. Vonbaeyer, *Phys. Rev. Lett.* 5, 223 (1960).
22. G.A. Slack, *Phys. Rev.* 105, 829 (1957).
23. B. Abeles, *Phys. Rev.* 131, 1906 (1963).
24. C. Rincón, M.L. Valeri-Gil, and S.M. Wasim, *Phys. Status Solidi (a)* 147, 409 (1995).
25. J.W. Shen, X.Y. Zhang, Z.W. Chen, S.Q. Lin, J. Li, W. Li, S.S. Li, Y. Chen, and Y.Z. Pei, *J. Mater. Chem. A* 5, 5314 (2017).
26. Y. Gelbstein, *J. Appl. Phys.* 105, 023713 (2009).
27. J. Navratil, T. Plechacek, C. Drasar, V. Kucek, F. Laufek, E. Cernoskova, L. Benes, and M. Vlcek, *J. Electron. Mater.* 45, 2904 (2016).